Optical darkness in short-duration γ-ray bursts

Caden Gobat[1]* (ID)

[1] Department of Physics, The George Washington University, 725 21st Street NW, Washington, DC 20052, USA

* Correspondence: cgobat@gwu.edu

Abstract: Gamma-ray bursts (GRBs) categorically produce broadband afterglow emission, but in some cases, emission in the optical band is less luminous than expected. This phenomenon, aptly dubbed "optical darkness", has been studied extensively in long GRBs (associated with hypernovae created by dying massive stars), with possible explanations ranging from host environment extinction to high redshift to possibly unique emission physics. However, investigations into optical darkness in short GRBs—associated with two compact objects in a binary system spiralling together and merging—have thus far been limited. This work implements a procedure for determining the darkness of GRBs based on spectral indices calculated using temporally-matched *Swift*-XRT data and optical follow-up observations; presents a complete and up-to-date catalog of known short GRBs that exhibit optical darkness; and outlines some of the possible explanations for optically dark short GRBs. In the process of this analysis, we develop a versatile codebase that facilitates reproducibility and scalability of the data processing pipeline. These analysis tools and resulting complete sample of dark short GRBs enable a systematic statistical study of the phenomenon and its origins, and reveal that optical darkness is highly dependent on observing response time and observational effects.

1. Introduction

Gamma-ray bursts are powerful astrophysical explosions that constitute some of the brightest transient phenomena observed in the universe. The prevailing hypothesis is that GRBs are the result of one of two main classes of progenitor: either collapsar events, resulting from core collapse in dying supermassive stars, or the merging of two compact objects (neutron stars or possibly black holes) that once orbited one another in a binary system. Observationally, GRBs are generally split into two subpopulations (Kouveliotou et al., 1993) corresponding to these two progenitor types on the basis of the burst's T_{90} duration, the time it takes for it to emit 90% of its energy.[1] "Short" GRBs, typically associated with binary neutron star mergers,[2] are usually defined as those with $T_{90} \lesssim 2$ seconds, and "long" GRBs, resulting from core collapse events, are those with $T_{90} \gtrsim 2$ seconds. The split in the distribution of GRB durations is shown in Figure 1. Other

---

[1] T_{90} is defined by Kouveliotou et al. as the time it takes for the cumulative counts to increase from 5% to 95% above the background, thus encompassing 90% of counts within the observing band.

[2] Observational confirmation that binary neutron star mergers are linked to short GRBs came with the simultaneous observation of kilonova AT2017gfo, GRB 170817A, and gravitational wave event GW170817 (see LIGO Scientific Collaboration et al., 2017).
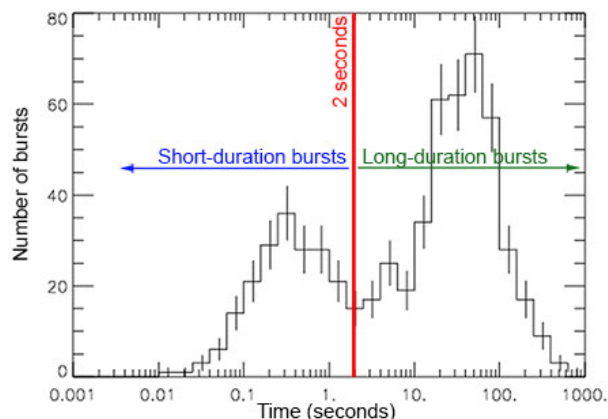
Figure 1: The bimodality in the GRB prompt emission duration distribution is evident. (Figure from NASA GSFC)

metrics are sometimes used to classify GRBs as well, such as properties of their spectra (short GRBs typically have harder spectra, meaning they produce relatively more emission at higher energies) and luminosity (long GRBs are typically much more luminous overall), when such data are available. For an in-depth review of gamma-ray bursts, see Gehrels et al. (2009).

Categorically, after the initial 'burst,' GRBs produce an afterglow, which refers to a period of fading emission that lasts from hours to days after the initial event. In 1997, van Paradijs et al. announced the discovery of the first optical counterpart to a GRB—that is, afterglow emission from a GRB at optical wavelengths, rather than only γ- and X-rays. Transient optical emission has now been associated with countless GRBs since. Shortly after this, however, Groot et al. (1998) reported on the discovery of a GRB with no detectable optical afterglow. Since then, observers have found that a fraction of all GRB afterglows exhibit a phenomenon known as optical darkness, where the afterglow as a whole is well-detected (typically in the X-rays) and yet much dimmer than expected in the optical band. This phenomenon, known as optical darkness, has been observed in both long and short GRBs (Greiner et al., 2011), with a number of proposed explanations. However, the implications of optical darkness differ somewhat for the two different classes of progenitor. The massive stars associated with long GRBs live fast and die young, while the short GRB binary systems must be old enough for both members to have gone supernova and turned into neutron stars, and then orbited each other for long enough to spiral in and collide.

One proposed explanation for why some GRBs are optically dark is that emission has been redshifted towards the infrared due to cosmological distance and the expansion of the universe, but this would imply that the event occurred long ago, when the Universe was relatively young. This explanation makes sense for long GRBs, which can reasonably be expected to be possible even in the early ages of the Universe. However, compact binary merger events should not be expected to occur at this early stage of the Universe's evolution, as they simply would not have had time to form. Another option is host galaxy extinction, (Lazzati et al., 2002; Covino et al., 2013; Littlejohns et al., 2015) which refers to the possibility that gas and dust within the distant galaxy where the GRB occurred selectively blocks light in the optical band. Again, this is perfectly

rational for long GRBs, which occur in hotbeds of star-forming activity amidst regions of dense gas and dust. However, this is not so universally applicable for short GRBs, whose progenitors often travel far away from where the stars formed, and are not as predictably found in these kinds of regions. A final theory is that optical darkness is an intrinsic property of certain GRBs: for some reason, some simply might not emit as much optical light as others. However, this unique physics explanation is disfavored for long GRBs (Rol et al., 2005). Partly due to these contrasts, and because of the overall difference in afterglow brightness of long and short GRBs, optical darkness in long GRBs has been studied much more extensively than in short ones. This work focuses on short GRBs in order to better understand the environments in which they form and the histories of the systems that produce them.

Whether or not a burst is empirically classified as optically dark is determined by the relative flux values at X-ray versus optical wavelengths. GRB spectra are classically modeled using power laws (i.e. $F_\nu \propto \nu^{-\beta}$, where β is known as the spectral index). If we can establish an idea of what the afterglow looks like between these two regions of the spectrum by calculating the optical-to-X-ray spectral index β_{ox}, we can determine whether a burst should be classified as optically dark.

This work implements a scalable pipeline for analyzing each burst in our sample to determine whether it meets the criteria for optical darkness according to two different methods (see §2.1), building on data published by Fong et al. (2015) and Rastinejad et al. (2021) with automatically retrieved X-ray spectra and lightcurves, as well as ultraviolet, optical, and near-infrared follow-up observations. Using this, we present a complete catalog of optically-dark short GRBs since *Swift*'s launch in 2004 (through May 2021), and offer insight into the mechanisms and possible causes of the phenomenon.

2. Methodology

2.1. Theory

The prevailing physical explanation for GRB emission is the fireball model (Piran, 1999), in which a primary radiation mechanism is synchrotron emission (Blumenthal & Gould, 1970) created when shock waves, composed mostly of electrons, traveling at different (relativistic) speeds collide with each other and the material surrounding the burst. The synchrotron radiation spectrum depends on the energy distribution of the Lorentz factors of electrons in the blast wave, which can be described by a power law with index p, i.e.

$$n_e(\gamma) \propto \gamma^{-p} \tag{1}$$

However, the synchrotron spectrum that arises from this electron distribution is not a simple power law, but instead has a break at a frequency known as the cooling break, ν_c, which arises from electron 'cooling' due to higher electron energy loss rates at higher frequencies. Figure 3 shows a prototypical broken power law afterglow spectrum with indices as they relate to p.

Because p is typically greater than 2, we expect the lower limit for the spectral index to be 0.5, if the cooling break is located above the observing frequency. However, there have been cases
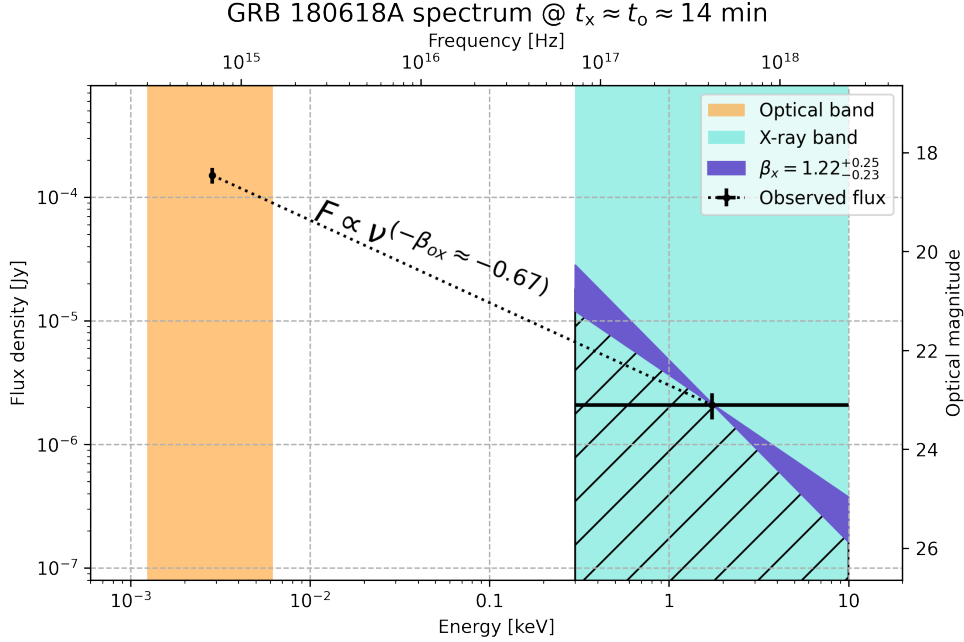
Figure 2: Visualization of an example end product for a pair of temporally-matched flux points for GRB 180618A just over 14 minutes post-trigger ($\Delta t_{\mathrm{ox}} = 2.7\%$). *Swift*-XRT reports integrated fluxes (black diagonal hashes) in the 0.3–10 keV band (shaded blue region), from which we compute spectral flux density (black data point on the right) using the X-ray spectral index (region of uncertainty in purple). We then convert an optical, ultraviolet, or infrared magnitude into a spectral flux density as well (black data point on the left) and use the two fluxes and their associated observing frequencies to calculate β_{ox} (Eq. 6). This particular case has $\beta_{\mathrm{ox}} = 0.67^{+0.09}_{-0.50}$ and $\beta_{\mathrm{x}} = 1.22^{+0.25}_{-0.23}$, meaning the X-ray spectral index is rather steep, and the optical-to-X-ray spectral index is somewhat shallower.

where $p < 2$ (for example, GRB 010222; see Masetti et al., 2001; Stanek et al., 2001), so this assumption may not be universally valid. Given this, the spectral index in the optical region is perhaps better judged relative to the spectral index in the X-ray region, rather than on a constant value cutoff. The predicted spectral index below the cooling break is $\frac{p-1}{2}$, and $\frac{p}{2}$ above it (see Fig. 3). If the cooling break ν_c is located between the X-ray and optical bands, we should thus expect the spectral indices at these two locations on the spectrum to differ by 0.5.

A small value of β_{ox} implies that the power law 'slope' between the optical and X-ray band is particularly shallow, or perhaps even positive (using the convention of $F_\nu \sim \nu^{-\beta}$, $\beta < 0$ implies a positive slope). There are two main criteria in use in the literature for determining optical darkness. The first (Jakobsson et al., 2004) defines darkness using a strict cutoff of $\beta_{\mathrm{ox}} < 0.5$, as they take the $p > 2$ assumption at face value. The second method (van der Horst et al., 2009) does not make such an assumption as to the value of p, and takes into account a burst's X-ray spectral information as well. Such data are increasingly available thanks to the rapid follow-up capabilities of the NASA Neil Gehrels *Swift* Observatory's X-ray Telescope (*Swift*–XRT, Burrows et al., 2005). If we know the spectral index in the X-ray regime (β_{x}), we can compare it to the optical-to-X-ray spectral index. van der Horst et al. thus define a burst as optically dark if $\beta_{\mathrm{ox}} < \beta_{\mathrm{x}} - 0.5$. Based on current physical models for GRB afterglow emission mechanisms, we expect to see $\beta_{\mathrm{x}} - 0.5 < \beta_{\mathrm{ox}} < \beta_{\mathrm{x}}$,
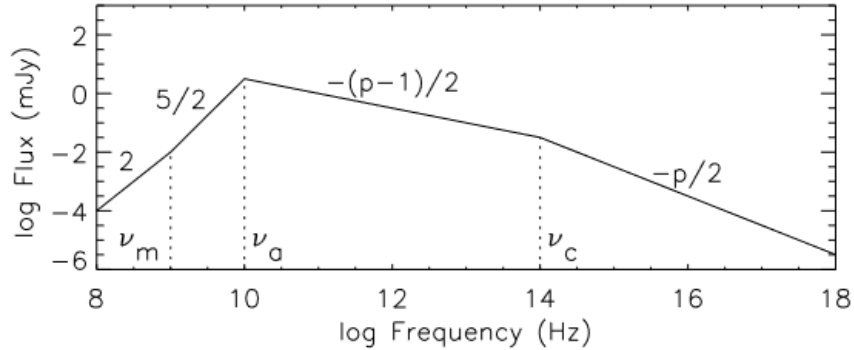
Figure 3: Schematic view of the effect of cooling break location (ν_{c}) and power law slopes to either side of it based on the value of p. (Figure from van der Horst, 2007).

depending on the exact location of ν_c at a given time. If β_{ox} is below this range, the burst should be considered optically dark.

2.2. Data/Observations

Our sample starts from the master-level *Swift* GRB table. From there, we select GRBs that meet one or more of the following critera:

- $T_{90} \leq 2$ seconds
- GRB appears in data tables of Rastinejad et al. (2021) or Fong et al. (2015)
- A keyword such as "short burst", "short/hard", "short GRB", etc. appears on the burst's corresponding GCN Circular page and is then manually verified

This provides a table with a list of GRB identifiers as well as basic information about the bursts. The calculation of β_{ox} requires contemporaneous flux measurements in the X-ray and optical bands. The UK *Swift* Science Data Center (UKSSDC; Evans et al., 2007, 2009) provides an online repository comprising X-ray data from *Swift*-XRT. To collect these data, we wrote custom, automated scripts to query the online repository (§2.3) to scrape spectrum pages for X-ray photon indices ($\Gamma = 1 + \beta_{\mathrm{x}}$) and intrinsic hydrogen column densities, N_H. We parse the lightcurve pages to obtain X-ray flux timeseries, and the XRT Live Catalog pages for the fitted temporal indices (α) and corresponding lightcurve break times.

The majority of our optical, infrared, and ultraviolet data were collected manually from GCN Circular announcements of follow-up observation results for GRBs of interest. In recent years, GRB localizations published through the Gamma-ray burst Coordinates Network (GCN) have enabled increasingly efficient and rapid follow-up observations by telescopes around the world. By compiling data from the GCN Circulars for each of the bursts in our sample, we compile a table of magnitudes of optical detections, upper limits, and associated errors, as well as the observation time and observing instrument/band. We include optical detection and upper limits published via GCN Circular for all bursts in the sample.

Also included are X-ray and optical data from Fong et al. (2015) and Rastinejad et al. (2021), as well as a few other publications which are cited in the data on an individual basis.

5

2.3. Code/Data analysis

After generating the required catalogs (general sample information, Table A1; optical observations, Table A3; and X-ray lightcurves, Table A2), we process it using a custom, generalized software pipeline that performs the appropriate conversions, matches optical and X-ray data points in time, and calculates darkness according to both methods, all while automatically handling error propagation and uncertainty in a statistically robust way. The pipeline was implemented in Python, with several distinct, consecutive sections.

2.3.1. X-ray data processing

The UKSSDC provides *Swift*-XRT lightcurves for GRBs in units of bolometric (integrated) flux in the 0.3–10 keV band. To compare fluxes at specific wavelengths, it is necessary to convert these integrated fluxes into spectral flux densities (i.e. energy per time per area per frequency; units of Jansky or similar). Within the X-ray band, we assume the afterglow spectrum to be described by a power-law with spectral index β_x.[3] This yields the following relation:

$$F_x = \int_{0.3 \text{ keV}}^{10 \text{ keV}} F_E \, dE = C \int_{7.3 \cdot 10^{16} \text{ Hz}}^{2.4 \cdot 10^{18} \text{ Hz}} \nu^{-\beta_x} \, d\nu \tag{2}$$

where F_x is a bolometric flux value from *Swift* and C is a scaling coefficient that accounts for the X-ray luminosity and distance from the burst. The value of C can be determined via the analytical solution to (2), which is

$$F_x = C \cdot \begin{cases} \frac{\nu^{1-\beta}}{1-\beta} & \text{if } \beta_x \neq 1 \\ \ln(\nu) & \text{if } \beta_x = 1 \end{cases} \Bigg|_{7.3 \cdot 10^{16} \text{ Hz}}^{2.4 \cdot 10^{18} \text{ Hz}} \tag{3}$$

With a value for C, we evaluate $C\nu^{-\beta_x}$ at $E = 10^{\frac{\log(10)+\log(0.3)}{2}}$, the logarithmic mean frequency of the 0.3–10 keV range, to get $F_{\nu,x}$, the spectral flux at the logarithmic midpoint of the X-ray band (see Fig. 2, where the hashed region represents the bolometric flux integral, which has units of energy per time per area with no spectral component, and the point on the right is the derived spectral flux). We perform this computation on every entry on the XRT data table (typically several tens of data points for each GRB) to compute a usable spectral flux for each.

2.3.2. Optical data processing

Essential information collected in the optical data table includes observation time (seconds post-GRB trigger), magnitude or magnitude limit, magnitude error, observation filter and its effective wavelength λ_{eff}, and the reddening, E_{B-V}, which describes of the amount of interstellar material within our galaxy in our line of sight to the burst.

---

[3]While there is a slight possibility that the X-ray spectral index changes over time, this evolution is typically negligible, so we take the single value of β_x determined from the time-averaged X-ray spectrum to be a constant for each burst.
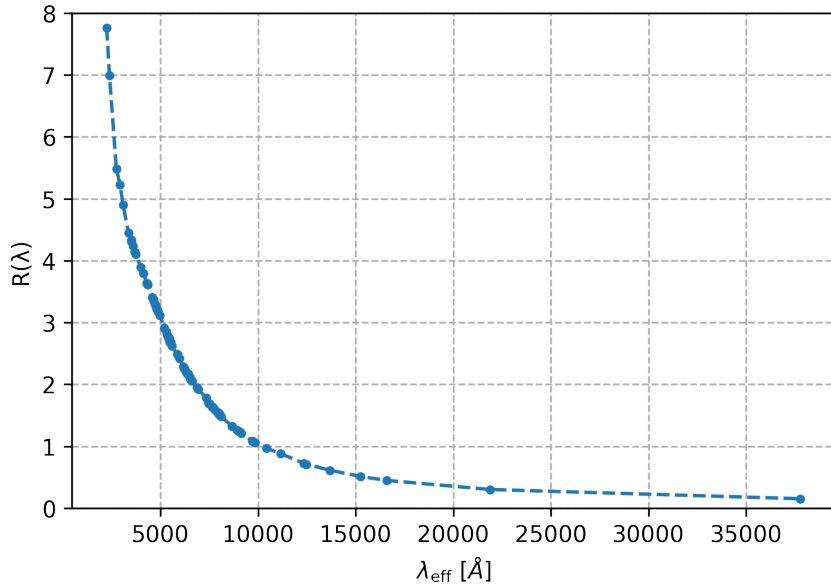
Figure 4: Relationship between observing wavelength and coefficient to convert between E_{B-V} reddening and magnitude extinction.

From here, we correct for galactic extinction—the attenuation of light intensity due to it passing through gas and dust in the galaxy. The extinction (A, in magnitudes) in a band with characteristic wavelength λ is given by $A_\lambda = R_\lambda \cdot E_{B-V}$, where R_λ is a scaling coefficient dependent on λ, since shorter wavelengths of light are more strongly absorbed by interstellar material. To calculate this, we establish an interpolatory function using empirical extinction data provided in Table 6 of Schlafly & Finkbeiner (2011). The relationship is well-defined, as shown in Fig. 4. Knowing this and the reddening value for each GRB we calculate galactic extinction and adjust our magnitude values for it.

With all of this information, we then calculate a spectral flux or upper limit for the observation (using the AB magnitude system) through the formula

$$F_{\nu,\mathrm{o}} = 3631 \cdot 10^{-\frac{m_{\mathrm{AB}} - A_\lambda}{2.5}} \ \mathrm{Jy} \tag{4}$$

2.3.3. Temporal matching & calculation of β_{ox}

With unit-compatible flux values in the X-ray and optical bands, the next step is to match these data points in time. We define the percentage temporal separation as

$$dt_\% = \frac{|t_{\mathrm{o}} - t_{\mathrm{x}}|}{t_{\mathrm{x}}} \tag{5}$$

and calculate this for every combination of optical and X-ray data points within each GRB, accepting any pair of data points for which $dt_\% \leq 0.2$ as a candidate match.

For each temporal match of X-ray and optical data, we calculate β_{ox}, the power-law slope between the two points:

$$\beta_{\mathrm{ox}} = -\frac{\log(F_{\nu,\mathrm{x}}/F_{\nu,\mathrm{o}})}{\log(\nu_{\mathrm{x}}/\nu_{\mathrm{o}})} \tag{6}$$

Because this calculation assumes exactly contemporaneous flux observations in the two bands, we must account for some additional error due to time-dependent afterglow decay. We use the X-ray temporal decay index α (such that $F_{\mathrm{x}}(t) \propto t^{-\alpha}$; also retrieved from the UKSSDC online repository) to calculate the additional error due to the separation in time that does exist using the formula

$$\Delta\beta_{\mathrm{ox}} = |\alpha \log(1 + dt_\%)| \tag{7}$$

and combine this error with the propagated uncertainty on β_{ox} already. For each matched pair and resultant β_{ox}, we set a boolean flag for optical darkness according to the Jakobsson et al. method if $\beta_{\mathrm{ox}} < 0.5$, and one for the van der Horst et al. method if $\beta_{\mathrm{ox}} < \beta_{\mathrm{x}} - 0.5$. This produces our resulting population of dark short GRBs.

2.3.4. Error & uncertainty propagation

Each stage of the pipeline described above involves quantities that each have an associated uncertainty. In many cases, this uncertainty is asymmetric (i.e., the error in the positive direction differs from the error in the negative direction). To ensure proper handling and propagation of all of these uncertainties, we have developed a stand-alone Python library for representing these kinds of numbers. The `AsymmetricUncertainty` class provides a novel object type for representing numbers in the form $\mathtt{nominal}^{+\mathtt{pos}}_{-\mathtt{neg}}$ that behave appropriately under all standard mathematical operations (addition, multiplication, exponentiation, etc.), and can be combined with one another using such operations to propagate associated uncertainties. Each instance of the `AsymmetricUncertainty` class is treated as two conjoined Gaussian probability distribution halves, described by

$$P(x, \mu, \sigma_-, \sigma_+) = \frac{\sqrt{2}}{\sqrt{\pi}(\sigma_- + \sigma_+)} \cdot \begin{cases} \exp\left(-(x-\mu)^2/2\sigma_-^2\right) & x < \mu \\ \exp\left(-(x-\mu)^2/2\sigma_+^2\right) & x > \mu \end{cases} \tag{8}$$

Notable examples of quantities in this analysis that have asymmetric uncertainties are X-ray flux, observation time, and spectral index (F_{x}, t_{x}, and β_{x}). This means that each β_{ox}—the computation of which involves all of these values—also has an asymmetric uncertainty. The `AsymmetricUncertainty` class is also equally capable of handling classical symmetric uncertainties ($\mathtt{pos} = \mathtt{neg}$), as well as upper/lower limits ($\mathtt{nominal}^{+0}_{-\infty}$ or $\mathtt{nominal}^{+\infty}_{-0}$, respectively), making it a versatile computational tool.

3. Results

The original sample of short *Swift* GRBs consisted of 195 events, spanning from February 2005 through the end of 2021. Of these, we obtain an X-ray lightcurve for 158 and at least one optical observation for 143. The overlap between these two sets (i.e., the number of bursts for which we had both X-ray and optical data) was 138. Of these, 101 bursts had at least one temporally matching set of data points with $dt_\% \leq 0.2$, which comes out to 6.1 ± 0.5 candidate GRBs per

year of the sample. Finally, 50 bursts had at least one match that qualified as optically dark by at least one of the methods described above, yielding an average rate of 2.9 ± 0.4 empirically 'dark' short bursts per year, a rate of approximately $48\% \pm 8\%$ of eligible bursts are nominally dark at some point by one or both methods. The number of bursts per year is shown in Fig. 5.
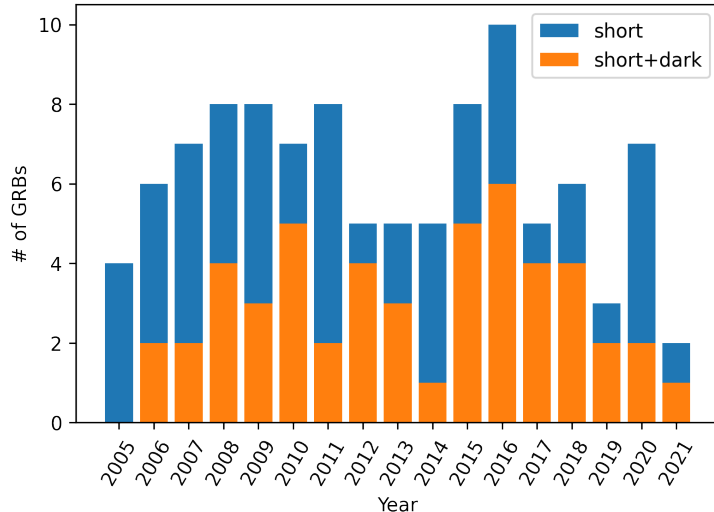

Figure 5: Bursts per year in our sample as a whole as compared to bursts per year that have at least one matched data pair that qualifies as dark by one or both methods.

However, the vast majority of these 'dark' points come from very early-time follow-up observations. We can observe this effect in the population as a whole by studying the time distributions of optical observations that constitute dark pairs versus not dark data pairs. Discrete classification of observation times and the breakdowns are given in Table 1 and shown to have a dependent relationship on darkness classification. Continuous distributions of observation times split by darkness classification are shown in Fig. 6.

t_o	Not dark	Dark
<5 min	37	52
5–50 min	183	64
>50 min	657	25

Table 1: Crosstabulation of darkness (by one or both methods) with optical observations across all matched GRBs showing the impact of observation time. Early-time observations are disproportionately dark: a contingency test on this table yields $\chi^2 \cong 238$ (2 dof) with $p \approx 0$ to within machine precision, indicating that an observation's classification as dark or not is highly dependent on the time after the trigger at which the data are taken.

To illustrate this effect quantitatively, we perform a search for events that have a calculated dark point at later times. We find 23 such bursts with a dark point at $t - t_0 > 5$ minutes (300 seconds), and only 10 with an optically dark point at $t - t_0 > 50$ minutes (3000 seconds).
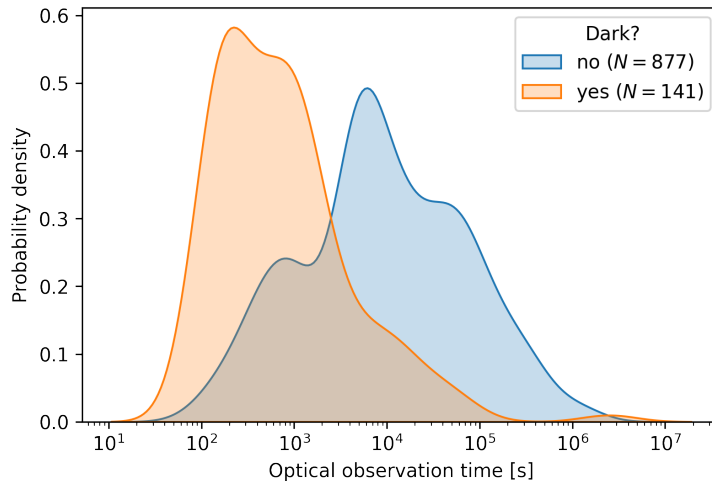
Figure 6: Kernel density plot showing the distribution of all optical observation times for dark data pairs and not dark data pairs. Visually, these distributions are clearly not analogous, and a Kolmogorov-Smirnov (K-S) test confirms this: we get a statistic of $D = 0.59$ with $p \approx 0$, showing with nearly 100% confidence that the two do not come from the same parent distribution.

The complete results of this study can be visualized in Fig. 7, which shows the distributions of β_x and β_{ox} relative to one another at the darkest (lowest value of β_{ox}) matched point for each GRB. This plot may therefore skew somewhat 'dark', as it has not been corrected for the early-time anomalies discussed above. Interestingly, we note a peak in the distribution of β_{ox} just below 0.5, which is Jakobsson et al.'s cutoff for defining optical darkness.

4. Discussion

Our preliminary finding that just under half of short bursts exhibit optical darkness is unexpected, as previous studies (Rol et al., 2005; Greiner et al., 2011; Littlejohns et al., 2015) have found a similar fraction for long GRBs, and we would expect short GRBs to not be as categorically dark. There are a number of possible reasons for this unexpected initial result.

4.1. Early-time X-ray anomalies

Swift's short response time in combination with the number of currently operational ground-based observatories capable of performing rapid follow-up often results in simultaneous observational coverage of GRB afterglows in the optical and X-ray bands. Because it is entirely possible for afterglow emission in the X-ray and optical bands to fade over time at different rates (Greiner et al., 2011), the resulting value of β_{ox} can change over time as well, even when looking at a single burst.[4] As discussed in §3, we note numerous cases where a burst qualifies as dark at early times, but then not at later ones.

---

[4]If the temporal decays of the optical and X-rays paralleled one another exactly, they would always be the same distance apart in logarithmic space, resulting in a constant value of β_{ox}.
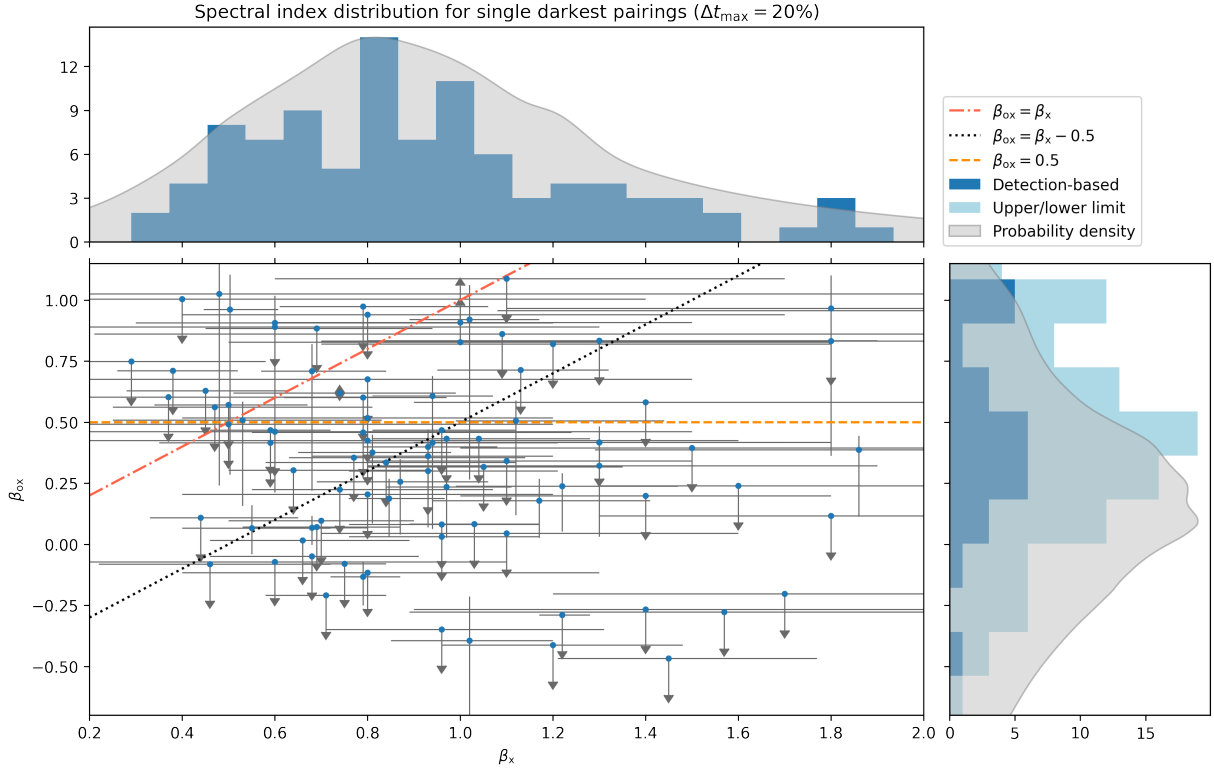
Figure 7: Each point in the plot above represents one burst and corresponds to the minimum value of β_{ox} for that GRB. Lines are drawn at various β_x–β_{ox} relations of interest (the van der Horst et al. definition of darkness is shown in dotted black, while the Jakobsson et al. criterion is the dashed yellow line). Top and side plots show distributions for each variable created from sums of asymmetric pseudo-normal probability distribution functions based on the error bars of each point (see §2.3.4).

To investigate the effects of observation time on perceived optical darkness, we inspected dark bursts' individual lightcurves, and noted that many such points where $\beta_{ox} < 0.5$ or $\beta_{ox} < \beta_x - 0.5$ (or both) were at times when there is clearly atypical behavior occurring in the X-rays. The canonical behavior for the temporal evolution of the X-ray afterglow (Nousek et al., 2006) is a brief period of very steep decay, followed by a shallow decay, and then finally a decay with an intermediate slope. When the actual behavior differs significantly from this expectation, we thus violate our assumption about how the X-rays "should" behave, even in comparison to the optical band. Therefore, we hypothesize that many of these early points are dark by technicality, but not necessarily because of low optical flux in a physically meaningful way—for example, an X-ray excess is just as capable of causing β_{ox} to be shallow. The lightcurves of GRBs 161004A and 170822A (Fig. 8) provide particularly notable examples of this, with an early X-ray flare and an extended plateau, respectively.

We therefore conclude that, although bursts like this may qualify as optically dark in the numerical sense, it is often not in the interesting sense of the phenomenon that we are seeking. There are a number of possible reasons for this anomalous X-ray behavior at early times. There is a chance that *very* early X-ray observations could be catching the tail end of the burst's prompt
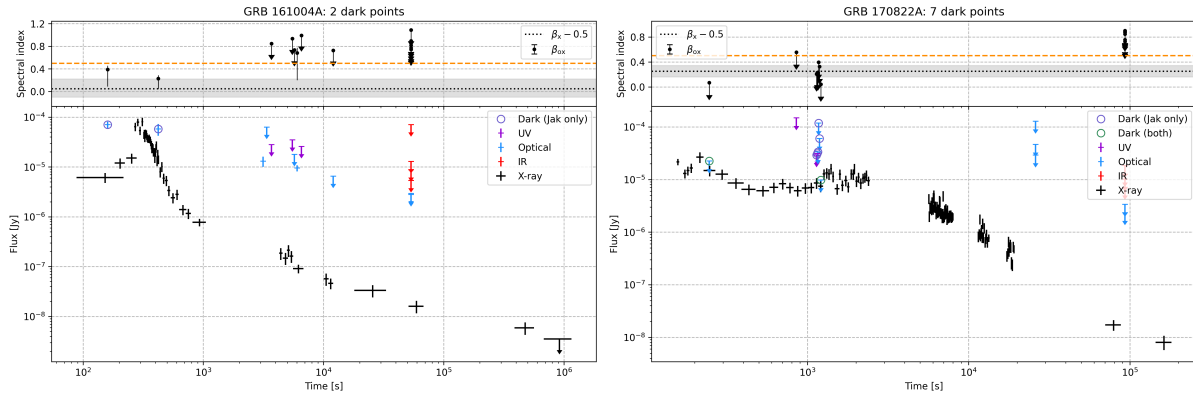
Figure 8: In the light curve of GRB 161004A on the left, we note an obvious X-ray flare (also flagged by the automated *Swift*-XRT light curve fitting routine; Evans et al., 2007, 2009) that peaks around $\delta t \approx 300$ seconds, causing optical points at $\delta t = 160$s and $\delta t \approx 420$s to appear dark, even though the optical behavior looks fairly canonical. Similarly, we observe plateau-like behavior (and possibly a flare) evident in the light curve of GRB 170822A on the right, lasting until around 2000 seconds post-trigger. Both are cases of anomalous X-ray behavior where it is clear that the light curve has not settled into 'normal' decay, meaning that standard assumptions about emission mechanisms are not applicable.

emission or prolonged central engine activity. Regardless of whether the merger product is a rapidly spinning supra-massive neutron star, or collapses immediately into a black hole, we expect that not all of the matter from the two progenitor objects will be consumed immediately—there is likely a short-lived accretion disk still actively fueling relativistic jets within the first few seconds or minutes after the burst. Our current physical understanding of GRB afterglows is that emission arises from external shocks between the burst outflow and material in the surrounding environment. To explain the 'extra' emission in the X-rays, we need an additional emission component beyond a standard forward shock afterglow model, and this could be the result of a number of theorized mechanisms, including internal shocks, magnetic reconnection, or a reverse shock scenario. This is because there are also interactions within the jet structure that must be considered: for example, a faster-moving blast wave behind the main shock front may eventually catch up with it and inject additional energy. Once this has all played out, however, we observe the X-ray lightcurve settle in to more typical behavior in time.

4.2. Short GRBs with extended emission

In the process of our analysis, the question of the nature and composition of our sample inevitably came up. Because of our methodology for selecting it, there are a number of sample members that do not obey the $T_{90} \leq 2$ second criteria. In fact, many of these have prompt durations on the order of tens or hundreds of seconds. These are bursts with what is known as extended emission, where high-energy emission continues beyond the main peak of the burst. The natural question, of course, is what sets these bursts apart and why. Fig. 1 shows the fractions of dark bursts on either side of $T_{90} = 2$ sec line. Of note is the fact that the two peaks of this histogram each appear to be fairly nice log-normal distributions, which reaffirms that our sample selection

methodology is reasonable, and suggests the possibility that short bursts with extended emission (EE) form a distinct class with a different physical origin than typical short GRB progenitors.
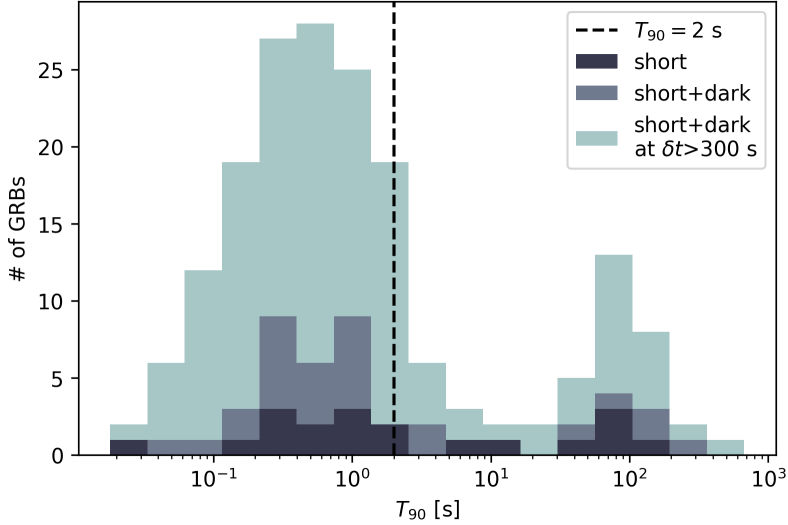

Figure 9: Histogram of T_{90} values for bursts in our sample. The vertical line shows $T_{90} = 2$s, the typically accepted value for defining the split between long- and short-duration GRBs. While the majority of events in our sample obey this, we also have some bursts that we deem to belong to the short/hard class for other reasons, and lie to the right of this diving line. We note an apparent bimodality of this histogram, with the two peaks separated at approximately $T_{90} = 20$s.

To probe whether these EE bursts arise from a different physical process, we examined the rates of optical darkness and late-time optical darkness on either side of the T_{90} cutoff. We count the number of bursts on either side of the this split, and compare that with relative fractions of bursts optically dark data points as well as bursts with dark data points at late time (e.g. $\delta t > 300$ seconds). If we find significantly different fractions of optical darkness or late-time optical darkness, we might infer that EE bursts (those in our sample but with comparatively large values of T_{90}) might be physically distinct from typical short bursts in their origins. The results of this analysis are shown in Table 2. While these numbers may hint at this (with extended emission bursts possibly being more optically dark than standard short bursts), when we incorporate and propagate uncertainties (Poisson statistics; $\sigma_N \approx \pm\sqrt{N}$), the fractions' errors overlap such that all of the numbers are compatible across each row, meaning we cannot conclude anything of significance.

	$T_{90} > 20$s	$T_{90} \leq 20$s	$T_{90} > 2$	$T_{90} \leq 2$
dark at $\delta t > 300$s	5 (17 ± 8 %)	14 (9 ± 3 %)	7 (15 ± 6 %)	12 (9 ± 3 %)
dark at any time	10 (34 ± 13 %)	36 (24 ± 4 %)	14 (29 ± 9 %)	32 (24 ± 5 %)
entire sample	29 (100%)	151 (100%)	48 (100%)	132 (100%)

Table 2: In parentheses are the fraction of the column total that each entry represents. Of note would be a rate that different significantly for bursts above one of the T_{90} values vs. below it. We choose two different cutoffs for defining EE bursts: $T_{90} = 2$ seconds, which is the classical criteria used for defining short bursts, and $T_{90} = 20$ seconds, which is the apparently more natural split in Fig. 9. However, this distinction does not make much difference.

Various studies (Troja et al., 2008; Gompertz et al., 2020) have suggested that EE short bursts are the result of neutron star/black hole binary mergers, as opposed to binary neutron stars. This is supported by physical modeling, as well as the fact that EE bursts are typically found closer to their host galaxies than non-EE bursts. This is notable because if true, it could reasonably be expected to contribute to optical darkness as well. Although our results hint at this possibility as well, larger number statistics are required to draw any significant conclusions.

4.3. Meaningfully dark bursts

The early-time effect (§4.1) is so widespread that when we correct for it, we find only 4 bursts that exhibit "meaningful" optical darkness: GRBs 060121, 090423, 130603B, and 170728B.

4.3.1. GRB 060121

We find that GRB 060121 attains a minimum optical-to-X-ray spectral index of $\beta_{\mathrm{ox}} \cong 0.18^{+0.09}_{-0.15}$ at $\delta t \approx 3.9$ hr. Its most likely redshift is $z \sim 4.6$, with a possibility that it might be $z \sim 1.7$ (de Ugarte Postigo et al., 2006). Either way, this qualifies it as fairly high-redshift (especially for a short GRB), meaning that it occurred long ago and far away. Because of the expansion of the universe, as light travels from a source to us here on Earth, photons' wavelengths are "stretched" by a factor of $(1 + z)$. Redshift is a potential contributor to optical darkness through a phenomenon known as the Lyman-α forest: individual clouds of neutral hydrogen between us and the source that would normally produce a single spectral absorption line or set of lines (primarily from the Lyman-α transition, which produces a line in the ultraviolet, at $\lambda_{\mathrm{rest}} = 121.6$ nm) are distributed more or less isotropically along the path between us and the source. Each of these clouds' absorption lines is also redshifted to a longer wavelength corresponding to its own cosmological distance. From our observer's perspective, this produces a "forest" (Weinberg et al., 2003) of lines that effect observed emission at wavelengths between $\lambda_{\mathrm{Ly}\alpha}$ and $(1 + z) \cdot \lambda_{\mathrm{Ly}\alpha}$.

Though it has a prompt duration of $T_{90} = 1.97 \pm 0.06$ seconds, Dichiara et al. (2021) find evidence that it also had extended emission, possibly incriminating whatever physical process gives rise to that phenomenon as possibly involved in this as well.

4.3.2. GRB 090423

GRB 090423 was and is one of the highest-redshift GRBs ever detected, at $z \sim 8.2$ (Tanvir et al., 2009; Salvaterra et al., 2009). Using typical values for cosmological parameters like the Hubble constant and density of the universe (Bennett et al., 2014), we realize that this z corresponds to a cosmological age of only about 600 million years—over 13 billion years ago. The associated luminosity distance is $\mathcal{D}_L \cong 80$–90 Gpc, or 260–290 billion light years. Though it is darkest at early times ($\beta_{\mathrm{ox}} < -0.21$ at $\delta t = 152$ s), the dark point at $\delta t \approx 55$ min is an upper limit of $\beta_{\mathrm{ox}} < 0.38$.

When the burst happened, its initial classification as long or short was inconclusive. While the T_{90} duration (10.3 ± 1.1 seconds in the observer frame, 1.1 ± 0.1 seconds in the GRB rest frame), spectral lag, and peak energy were consistent with a short burst (Krimm et al., 2009; Zhang et al., 2009, which is why it is present in our sample), it has since been confirmed to be a high-redshift
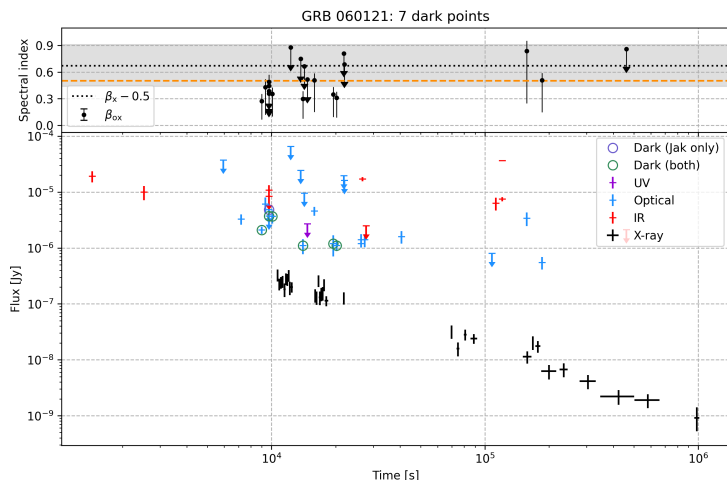
Figure 10: Multi-wavelength afterglow light curve of GRB 060121, showing optical darkness between approximately $\delta t = 10000$ sec and $\delta t = 20000$ sec. The optical and nIR observations that qualify as optically dark were taken by the Liverpool telescope in $r'i'z'$, OSN in RI, and the CAHA 2.2m and Bok 2.3m telescopes in R.

long GRB, which explains its optical darkness: at a redshift of $z \sim 8.2$, the Lyα forest would span wavelengths from 121.6 nm to 1119 nm—in other words, the entire optical band.
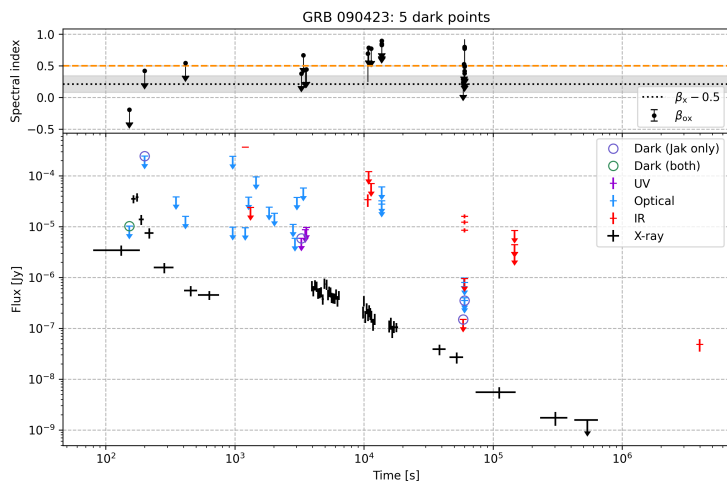

Figure 11: This light curve shows very early-time optical darkness in GRB 090423, possibly resulting from an apparent X-ray flare that peaks between $\delta t = 100$s and $\delta t = 200$s. However, it is also dark at later times (in UV at $\delta t \approx 3000$s—a *Swift*/UVOT upper limit—and in optical/nIR at $\delta t \approx 60000$s, from GMOS and GROND).

4.3.3. GRB 130603B

With $T_{90} = 0.18 \pm 0.02$ seconds, GRB 130603B lies solidly in the short class of γ-ray bursts. Spectroscopic analysis by de Ugarte Postigo et al. (2014) assigns a redshift of $z \sim 0.36$, ruling out redshift as a viable explanation for optical darkness in this case. Of interest, however, is the late-time excess X-ray emission noted by Fong et al. (2014), which they attribute to a rapidly

spinning supra-massive magnetar merger product. As the spin period of the magnetar increases, the lost angular momentum is radiated as energy through electromagnetic radiation. Fong et al. found that both the late time ($\delta t \gtrsim 3000$ s) spectrum and light curve of GRB 130603B were consistent with this model.

In the light curve for GRB 130603B (Fig. 12), we note that our optically dark points occur around this time as well (we find a minimum $\beta_{\rm ox} = 0.23^{+0.07}_{-0.21}$ at $\delta t \approx 1$ hr), indicating that the X-ray excess due to central engine/magnetar emission may be to blame for shallow values of $\beta_{\rm ox}$.
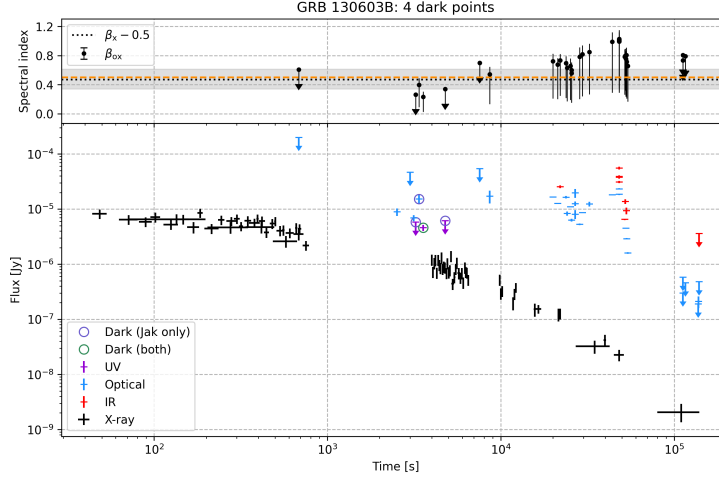

Figure 12: We identify a cluster of optically dark data points around $\delta t \approx 1$ hr, around the time that Fong et al.'s magnetar model takes over and excess X-ray emission becomes a significant contributor.

4.3.4. GRB 170728B

There is very little published work on GRB 170728B. It is optically darkest at $\delta t = 16$ min with $\beta_{\rm ox} = -0.13^{+0.06}_{-0.11}$, though we also find an upper limit of $\beta_{\rm ox} < -0.014$ at $\delta t \approx 3.5$ hr. With a short, multi-peaked burst structure but a T_{90} of 47.7 ± 25.2 seconds, this burst can be considered a short burst with extended emission, like those discussed in §4.2. There is no identified host galaxy association.

5. Summary & Conclusions

We present a complete, systematic study of optical darkness in short GRBs, a phenomenon that has until now only been studied extensively in long GRBs. To this end, we present our complete, scalable, and (mostly) automated software pipeline, as well as a comprehensive catalog of short GRBs that comprises >3000 optical observations and >5500 X-ray data points from nearly 200 individual bursts.

Previous work on long GRBs has found a rate of optical darkness around half (Littlejohns et al., 2015, and references therein). While our initial result for short GRBs is consistent with this, many instances of optical darkness in our sample stem from early-time observations, and we determine that in most cases, an excess of X-ray emission is to blame, rather than any significant optical deficit. The classification of data points as optically dark or not depends heavily on how
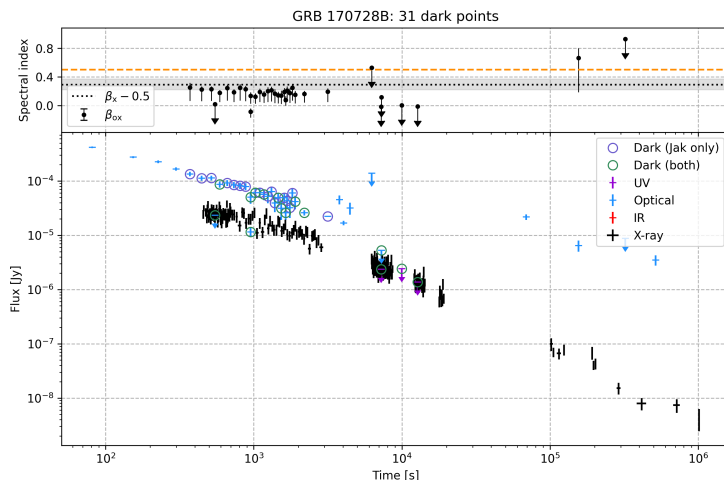
Figure 13: While the majority of the points that qualify as optically dark occur at early times, there is also a cluster of them around $\delta t \approx 10^4$ seconds that come from a series of *Swift*/UVOT upper limits.

quickly follow-up observations are obtained, and assessing optical darkness using existing criteria is better done at later times once X-ray emission has settled into regular decay. The high rate of occurrence of 'anomalous' early-time X-ray behavior suggests that the standard assumption of a purely synchrotron afterglow is not a complete picture. While previous studies of optical darkness in long GRBs have avoided this problem by consistently observing afterglows at later times, the comparatively faint overall nature of short GRB afterglows means that the availability of data skews earlier and identifying true optical darkness is more difficult.

When we account for early-time effects, we find that, as expected, optical darkness of real note is rarer in short GRBs than in long ones. We identify only 4 of our GRBs that are optically dark after the X-ray lightcurve has entered regular decay, and one of them is actually a long GRB. Because our eligible sample (of bursts with temporally-matched data) consists of 101 GRBs, this number represents a *true* optical darkness rate of less than 4%. To explain the optical darkness in these few individual cases, we turn to redshift, late-time X-ray excess, or the possibility of heterogeneity in short GRB progenitors, remnants, and environments that could cause discrepant afterglow behavior.

The tools and results presented here are structured so as to make updating and keeping the catalog up to date as straightforward as possible. In addition to newly developed computational tools with wide-ranging cross-disciplinary applicability, this work provides a robust framework for further investigation and analysis of optical darkness in both long and short GRBs alike, and constitutes another step towards a complete understanding of the physical origins of γ-ray bursts and the extreme processes of the universe.

References

Bennett, C. L., Larson, D., Weiland, J. L., & Hinshaw, G. 2014, ApJ, 794, 135, doi: 10.1088/0004-637X/794/2/135

Blumenthal, G. R., & Gould, R. J. 1970, Reviews of Modern Physics, 42, 237, doi: 10.1103/RevModPhys.42.237

Burrows, D. N., Hill, J. E., Nousek, J. A., et al. 2005, SSRv, 120, 165, doi: 10.1007/s11214-005-5097-2

Covino, S., Melandri, A., Salvaterra, R., et al. 2013, MNRAS, 432, 1231, doi: 10.1093/mnras/stt540

de Ugarte Postigo, A., Castro-Tirado, A. J., Guziy, S., et al. 2006, ApJL, 648, L83, doi: 10.1086/507868

de Ugarte Postigo, A., Thöne, C. C., Rowlinson, A., et al. 2014, A&A, 563, A62, doi: 10.1051/0004-6361/201322985

Dichiara, S., Troja, E., Beniamini, P., et al. 2021, ApJL, 911, L28, doi: 10.3847/2041-8213/abf562

Evans, P. A., Beardmore, A. P., Page, K. L., et al. 2007, A&A, 469, 379, doi: 10.1051/0004-6361:20077530

—. 2009, MNRAS, 397, 1177, doi: 10.1111/j.1365-2966.2009.14913.x

Fong, W., Berger, E., Margutti, R., & Zauderer, B. A. 2015, ApJ, 815, 102, doi: 10.1088/0004-637X/815/2/102

Fong, W., Berger, E., Metzger, B. D., et al. 2014, ApJ, 780, 118, doi: 10.1088/0004-637X/780/2/118

Gehrels, N., Ramirez-Ruiz, E., & Fox, D. B. 2009, ARA&A, 47, 567, doi: 10.1146/annurev.astro.46.060407.145147

Gompertz, B. P., Levan, A. J., & Tanvir, N. R. 2020, ApJ, 895, 58, doi: 10.3847/1538-4357/ab8d24

Greiner, J., Krühler, T., Klose, S., et al. 2011, A&A, 526, A30, doi: 10.1051/0004-6361/201015458

Groot, P. J., Galama, T. J., van Paradijs, J., et al. 1998, ApJL, 493, L27, doi: 10.1086/311125

Jakobsson, P., Hjorth, J., Fynbo, J. P. U., et al. 2004, ApJL, 617, L21, doi: 10.1086/427089

Kouveliotou, C., Meegan, C. A., Fishman, G. J., et al. 1993, ApJL, 413, L101, doi: 10.1086/186969

Krimm, H. A., Norris, J. P., Ukwatta, T. N., et al. 2009, GRB Coordinates Network, 9241, 1

Lazzati, D., Covino, S., & Ghisellini, G. 2002, MNRAS, 330, 583, doi: 10.1046/j.1365-8711.2002.05076.x

LIGO Scientific Collaboration, Virgo Collaboration, Fermi GBM, et al. 2017, ApJL, 848, L12, doi: 10.3847/2041-8213/aa91c9

Littlejohns, O. M., Butler, N. R., Cucchiara, A., et al. 2015, MNRAS, 449, 2919, doi: 10.1093/mnras/stv479

Masetti, N., Palazzi, E., Pian, E., et al. 2001, A&A, 374, 382, doi: 10.1051/0004-6361:20010740

Nousek, J. A., Kouveliotou, C., Grupe, D., et al. 2006, ApJ, 642, 389, doi: 10.1086/500724

Piran, T. 1999, PhR, 314, 575, doi: 10.1016/S0370-1573(98)00127-6

Rastinejad, J. C., Fong, W., Kilpatrick, C. D., et al. 2021, ApJ, 916, 89, doi: 10.3847/1538-4357/ac04b4

Rol, E., Wijers, R. A. M. J., Kouveliotou, C., Kaper, L., & Kaneko, Y. 2005, ApJ, 624, 868, doi: 10.1086/429082

Salvaterra, R., Della Valle, M., Campana, S., et al. 2009, Nature, 461, 1258, doi: 10.1038/nature08445

Schlafly, E. F., & Finkbeiner, D. P. 2011, ApJ, 737, 103, doi: 10.1088/0004-637X/737/2/103

Stanek, K. Z., Garnavich, P. M., Jha, S., et al. 2001, ApJ, 563, 592, doi: 10.1086/323941

Tanvir, N. R., Fox, D. B., Levan, A. J., et al. 2009, Nature, 461, 1254, doi: 10.1038/nature08459

Troja, E., King, A. R., O'Brien, P. T., Lyons, N., & Cusumano, G. 2008, MNRAS, 385, L10, doi: 10.1111/j.1745-3933.2007.00421.x

van der Horst, A. J. 2007, PhD thesis, University of Amsterdam

van der Horst, A. J., Kouveliotou, C., Gehrels, N., et al. 2009, ApJ, 699, 1087, doi: 10.1088/0004-637X/699/2/1087

van Paradijs, J., Groot, P. J., Galama, T., et al. 1997, Nature, 386, 686, doi: 10.1038/386686a0

Weinberg, D. H., Davé, R., Katz, N., & Kollmeier, J. A. 2003, in American Institute of Physics Conference Series, Vol. 666, The Emergence of Cosmic Structure, ed. S. H. Holt & C. S. Reynolds, 157–169, doi: 10.1063/1.1581786

Zhang, B., Zhang, B.-B., Virgili, F. J., et al. 2009, ApJ, 703, 1696, doi: 10.1088/0004-637X/703/2/1696

Appendix A Data tables

Table A1: Excerpt of short GRB sample properties.

GRB	*Swift* Trigger	T_{90} [sec]	z	β_X	N_H (intrinsic) [10^{21} cm^2]
211227A	1091101	83.79	—	$2.0^{+0.7}_{-0.6}$	$2.9^{+1.8}_{-1.5}$
211106A	GUANO	1.75	—	$0.1^{+1.06}_{-0.42}$	$0.0^{+3.43}_{-0.0}$
211023B	1080859	1.30	0.862	$1.12^{+0.23}_{-0.21}$	$0.9^{+0.6}_{-0.5}$
210919A	1073893	0.16	—	$1.1^{+3.3}_{-1.1}$	$1.1^{+24.7}_{-1.1}$
210726A	1061687	0.39	—	$1.2^{+0.32}_{-0.3}$	$2.9^{+1.3}_{-1.1}$
210704A	Fermi	4.7	<3.15	$0.5^{+0.6}_{-0.4}$	$0.0^{+1.62}_{-0.0}$
210618A	1056426	2.13	—	$1.6^{+2.2}_{-1.4}$	$5.8^{+13.4}_{-5.7}$
210413B	1043009	1.088	—	—	—
210410A	1042113	52.88	—	$0.45^{+0.18}_{-0.17}$	$0.4^{+0.6}_{-0.4}$
210323A	1038247	1.12	—	0.7 ± 0.2	$1.76^{+1.02}_{-0.89}$
210217A	1033264	4.22	—	$0.93^{+0.23}_{-0.22}$	$1.4^{+0.9}_{-0.8}$
210119A	1017711	0.06	—	—	—
201221D	1014037	0.16	1.046	$0.1^{+1.05}_{-0.47}$	$0.0^{+26.8}_{-0.0}$
201015A	1000452	9.78	0.425	1.1 ± 0.4	$6.0^{+7.0}_{-5.0}$
201006A	998907	0.49	—	$1.1^{+0.6}_{-0.5}$	$8.0^{+7.0}_{-5.0}$
200917A	996184	19.4	—	$1.33^{+0.25}_{-0.24}$	$9.5^{+2.3}_{-2.0}$
200907B	995004	0.83	—	0.8 ± 0.4	$1.4^{+2.9}_{-1.4}$
200826A	Fermi	—	—	$0.6^{+0.7}_{-0.6}$	$1.5^{+3.4}_{-1.5}$
200729A	984929	122.0	—	$0.37^{+0.26}_{-0.24}$	$9.2^{+3.3}_{-2.7}$
200716C	982707	86	—	$0.5^{+0.1}_{-0.06}$	$0.0^{+0.226}_{-0.0}$
200623A	GUANO	—	—	—	—
200522A	973628	0.62	0.4	$0.37^{+0.44}_{-0.27}$	$0.088^{+1.24}_{-0.088}$
200517A	MAXI	—	—	$0.74^{+1.32}_{-0.59}$	$0.24^{+2.89}_{-0.24}$
200512A	971846	74.0	—	$0.13^{+0.23}_{-0.22}$	$2.0^{+1.4}_{-1.2}$
200411A	965784	0.22	—	$0.68^{+0.23}_{-0.22}$	$1.3^{+0.9}_{-0.7}$
200409A	965484	17.91	—	$1.01^{+0.17}_{-0.16}$	$0.3^{+0.4}_{-0.3}$

NOTE — This table is available in its entirety in machine-readable form.

Table A2: Excerpt of short GRB X-ray light curve catalog.

GRB	δt [s]	X-ray flux [μJy]
211227A	$63.73^{+0.27}_{-0.25}$	$232.235^{+64.384}_{-57.996}$
211227A	$64.32^{+0.28}_{-0.32}$	$339.521^{+89.75}_{-80.209}$
211227A	$64.97^{+0.33}_{-0.37}$	$332.516^{+87.644}_{-78.003}$
211227A	$65.6^{+0.39}_{-0.3}$	$270.464^{+71.232}_{-63.363}$
211227A	$66.34^{+0.3}_{-0.35}$	$308.861^{+81.381}_{-72.555}$
211227A	$67.01^{+0.34}_{-0.37}$	$286.421^{+75.734}_{-67.795}$
	$\vdots$	
050509B	$270.67^{+1430.8}_{-208.97}$	$0.029^{+0.012}_{-0.009}$
050509B	$33148.22^{+26831.7}_{-27876.03}$	0.002 ± 0.001
050509B	$68301.53^{+8405.31}_{-5170.42}$	$0.008^{+0}_{-\infty}$

NOTE — This table is available in its entirety in machine-readable form.

Table A3: Excerpt of short GRB optical observation catalog. An error of 'UL' denotes an upper limit where the confidence was not specified.

GRB	Observatory	Instrument	Filter	λ_{eff} [Å]	δt [s]	m	σ_m	GCN	E_{B-V}
	OAN/SPM	RATIR	r	6149.31	111420	22.4	3-σ	30390	
			i	7531.29	111420	22.1	3-σ		
	Swift	UVOT	v	5411.43	62763	21.1	3-σ	30389	
	TNG	DOLoRes	r	6128.29	93312	22.13	0.13	30385	
	Assy-Turgen	AZT-20	r'	6141.12	81567.648	22.25	0.13	30384	
			r'	6141.12	338700.1	23.1	3-σ	30440	
	Calar Alto	2.2m	i'	7457.89	94423.104	21.84	0.13	30391	
		CAFOS	r	6520.18	177120	22.7	UL	30411	
	Gemini North	GMOS	K	21751.15	384480	22.9	0.3	30433	
			J	12746.62	475200	23.5	3-σ	30442	
210704A	GTC	OSIRIS	r	6350.01	96300	22.4	0.07	30392	0.007
			g'	4671.78	95385.6	22.42	0.11		
	OAJ	T80	r'	6141.12	96422.4	22.17	0.1	30401	
			i'	7457.89	94435.2	22.08	0.23		
			z'	8922.78	93398.4	21.5	UL		
	OAN/SPM	DDOTI	w	—	32400	19.7	5-σ	30383	
	SAO RAS	Zeiss-1000	R	6695.58	603298.37	23.1	0.3	30465	
			R	6695.58	772964.64	23.5	3-σ		
	NOT	ALFOSC	g'	4671.78	525744	23.78	0.11	30443	
			r'	6141.12	526694.4	23.27	0.09		
	OAN/SPM	DDOTI	w	—	12726	20.47	10-σ	30251	
			wh	3885.68	3803	20.4	3-σ		
			wh	3885.68	4112	21.1	3-σ		
210618A	Swift	UVOT	v	5411.43	4775	19.2	3-σ	30256	0.015
			b	4346.25	4191.5	20.5	3-σ		
			u	3520.95	3986	20	3-σ		
			w2	2085.73	4602	20.1	3-σ		
	OSN	1.5m	I	8565.14	587520	20.9	UL	30322	

NOTE — This table is available in its entirety in machine-readable form.